nature materials

SUPPLEMENTARY INFORMATION

DOI: 10.1038/NMAT4951

In the format provided by the authors and unedited.

Phase coexistence and electric-field control of toroidal order in oxide superlattices

A. R. Damodaran[1,2]*, J. D. Clarkson[1,2]*, Z. Hong[3], H. Liu[4], A. K. Yadav[1,2,5], C. T. Nelson[1,6], S.-L. Hsu[1,6], M. R. McCarter[7], K.-D. Park[8], V. Kravtsov[8], A. Farhan[9], Y. Dong[4], Z. Cai[10], H. Zhou[10], P. Aguado-Puente[11,12], P. García-Fernández[13], J. Íñiguez[14], J. Junquera[13], A. Scholl[9], M. B. Raschke[8], L.-Q. Chen[3], D. D. Fong[4], R. Ramesh[1,2,7], L. W. Martin[1,2]◆

[1] Department of Materials Science & Engineering, University of California, Berkeley, CA 94720, USA

[2] Materials Science Division, Lawrence Berkeley National Laboratory, Berkeley, CA 94720, USA

[3] Department of Materials Science and Engineering, Pennsylvania State University, State College, PA 16802, USA

[4] Materials Science Division, Argonne National Laboratory, Argonne, IL 60439, USA

[5] School of Electrical Engineering and Computer Science, UC Berkeley, Berkeley, California 94720, USA

[6] National Center for Electron Microscopy, Lawrence Berkeley National Laboratory, Berkeley, CA 94720, USA

[7] Department of Physics, University of California, Berkeley, Berkeley, CA 94720, USA

[8] Department of Physics, Department of Chemistry, and JILA, University of Colorado, Boulder, Boulder, CO 80309, USA

[9] Advanced Light Source, Lawrence Berkeley National Laboratory, Berkeley, CA 94720, USA

[10] X-ray Science Division, Argonne National Laboratory, Argonne, IL 60439, USA

[11] Centro de Física de Materiales, Universidad del País Vasco, 20018, San Sebastián, Spain

[12] Donostia International Physics Center, 20018 San Sebastián, Spain

[13] Departmento de Ciencias de la Tierra y Física de la Materia Condensada, Universidad de Cantabria, Cantabria Campus Internacional, avenida de los Castros s/n, 39005, Santander, Spain

[14] Materials Research and Technology Department, Luxembourg Institute of Science and Technology (LIST), 5 avenue des Hauts-Fourneaux, L-4362 Esch/Alzette, Luxembourg

*Contributed equally to this work

◆ lwmartin@berkeley.edu

Supplementary Information

1. Understanding short-period $(PbTiO_3)_n/(SrTiO_3)_n$ superlattice films ($n < 10$)

Synchrotron X-ray 3D-RSMs about various diffraction conditions were obtained for different period $(PbTiO_3)_n/(SrTiO_3)_n$ superlattices (n = 4-10) synthesized on $SrRuO_3$-buffered $DyScO_3$ (110) [$(001)_{pc}$, where *pc* indicates pseudocubic indices]. A 3D-RSM about the 002_{pc}-diffraction condition (Supplementary Fig. 1a) and its planar section (Supplementary Fig. 1b)

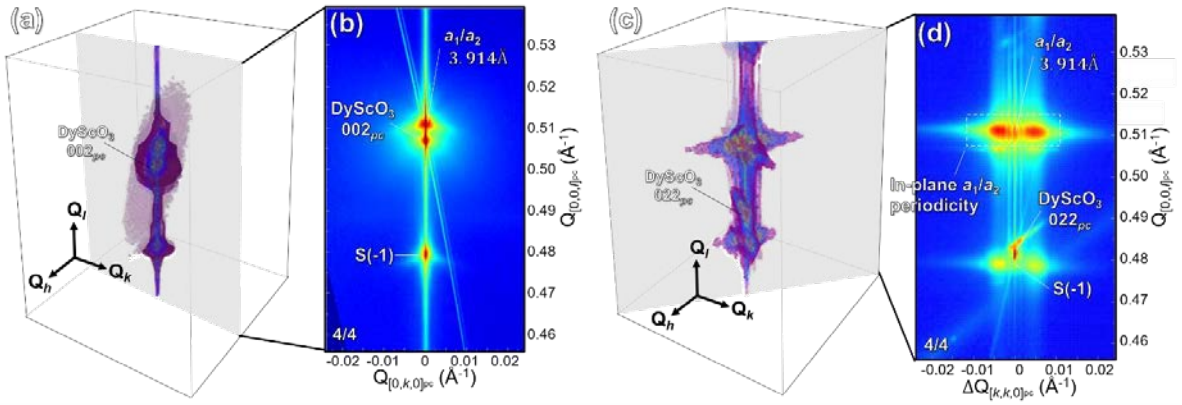

Supplementary Fig. 1. Synchrotron-based 3D-RSMs for a n = 4 superlattice about the **a,** 002_{pc}-diffraction condition of the $DyScO_3$ substrate, and **b,** a planar section of this 3D-RSM containing the in-plane $[010]_{pc}$ and out-of-plane $[001]_{pc}$ showing a single a_1/a_2 alloy peak and corresponding superlattice peaks. **c,** 3D-RSMs about the off-axis 022_{pc}-diffraction condition of the $DyScO_3$ substrate, and **d,** a planar section of this 3D-RSM containing the in-plane $[110]_{pc}$ and out-of-plane $[001]_{pc}$ showing a single a_1/a_2 alloy peak, corresponding superlattice peaks, and in-plane satellites corresponding to a domain periodicity of ~70 nm.

containing the in-plane $[010]_{pc}$ and out-of-plane $[001]_{pc}$ for the $n = 4$ superlattice reveals a single alloy film peak corresponding to an out-of-plane lattice parameter of 3.915 Å along with first- and higher-order superlattice reflections. Satellite peaks that arise from in-plane structural/polarization modulations are not observed around this diffraction condition. On the other hand, a 3D-RSM about the 022_{pc}-diffraction condition (Supplementary Fig. 1c) reveals a set of satellites along the in-plane $<110>_{pc}$ in addition to the film and superlattice reflections seen along the $[001]_{pc}$. These satellites are easily seen in the planar section of the 3D-RSM containing the in-plane $[110]_{pc}$ and out-of-plane $[001]_{pc}$ (Supplementary Fig. 1d), and correspond to a domain periodicity of ~70 nm in this direction. The fact that these satellites are absent for the 3D-RSM around the 002_{pc} diffraction conditions are indicative of the absence of an out-of-plane component of polarization modulation in these domains.

To characterize the nature of the in-plane polarization modulation in these films, we conducted *scanning probe-based lateral PFM studies*. The lateral PFM studies (Supplementary Fig. 2a) confirm the presence of ferroelectric domains with walls along the in-plane $[110]_{pc}$; a characteristic of in-plane polarized, tetragonal ferroelectric domains referred to as the a_1/a_2 phase. *Phase-field simulations* of the stable domain structure for the $n = 4$ superlattices also reveal the stabilization of ferroelectric a_1/a_2 stripe domains in the $PbTiO_3$ layers (Supplementary Fig. 2b) and are consistent with the experimental observations. The evolution of ferroelectric a_1/a_2 stripe domain width as a function of superlattice periodicity was extracted experimentally from synchrotron 3D-RSMs and also predicted using phase-field models (Supplementary Fig. 2c). An anomalous trend of decreasing domain width with increasing superlattice periodicity is observed. This corresponds to a region where Kittel's scaling is invalid and marks a regime where surface and interfacial effects dominate[1]. Kittel's law predicts a square root scaling of domain width for

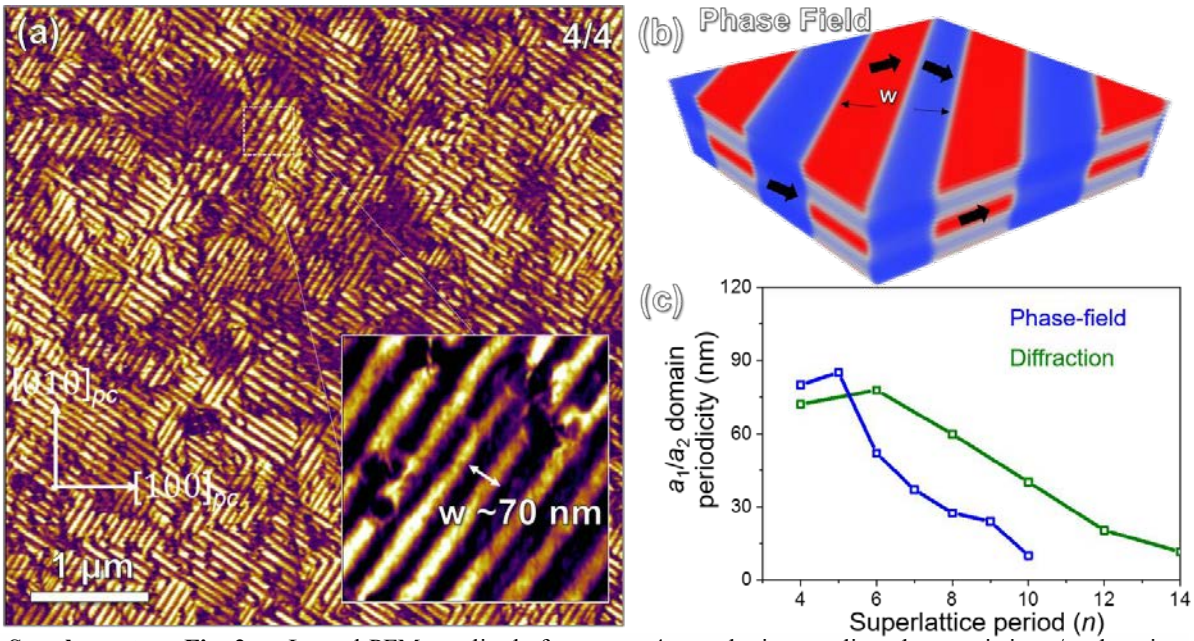

Supplementary Fig. 2. a, Lateral PFM amplitude for an $n = 4$ superlattice reveling characteristic a_1/a_2 domain structure, that is consistent with **b,** predictions from phase-field simulations. **c,** Comparison of the evolution a_1/a_2 domain width with superlattice periodicity ($n = 4, 6, \ldots$) measured from synchrotron X-ray diffraction studies (green curve) and corresponding predictions from phase-field simulations (blue curve).

ferroelectric/ferroelastic/ferromagnetic materials with film thickness, but hinges on assumptions including negligible domain wall thickness as compared to film thickness, and that surface effects are negligible. In the case of our $PbTiO_3/SrTiO_3$ superlattices with $n = 4$-15 unit cells, the thickness of individual ferroelectric layers are sufficiently small that such a breakdown of Kittel's law is not surprising. Instead, we observe ferroelastic a_1/a_2 twins in short-period superlattice films with an anomalous thickness scaling that is explained only by analytical theories that take into consideration the influence of interfaces and free surfaces on elastic strain fields within the film[1]. In this approach, the inhomogeneous internal stresses in strained polydomain epitaxial films were calculated by the method of fictitious dislocations distributed along domain boundaries and at the film/substrate interface. In turn, it was shown that the interaction between opposite surfaces/interfaces takes over below a critical thickness, and the domain size no longer decreases, but *increases* and diverges as the film thickness approaches zero.

2. Understanding intermediate-period $(PbTiO_3)_n/(SrTiO_3)_n$ superlattice films ($12 < n < 20$)

Synchrotron 3D-RSMs about the 002_{pc}-diffraction condition and its planar section containing the in-plane $[010]_{pc}$ and out-of-plane $[001]_{pc}$ for the $n = 16$ superlattice (Supplementary Fig. 3a & b, respectively) reveals significantly enhanced complexity. In addition, to the a_1/a_2 alloy peak along with first- and higher-order superlattice reflections, an extra set of film and superlattice peaks corresponding to the vortex phase are observed. Furthermore, satellite peaks from the in-plane ordering of clockwise and anticlockwise polarization vortices are also observed in the vortex phase with an in-plane periodicity of ~11 nm along $<100>_{pc}$. At the same time, 3D-RSM studies about the 202_{pc}-diffraction condition (Supplementary Fig. 3c) reveal satellites along the in-plane $<100>_{pc}$ arising from the vortex periodicity, as well as along the in-plane $<110>_{pc}$ (Supplementary Fig. 3d) corresponding to a_1/a_2 domain periodicity of ~13 nm. Such features in the 3D-RSMs are manifestations of the complex phase coexistence (refer main text, Fig. 2).

High-resolution TEM studies of these intermediate period superlattices were conducted to observe the vortex phase. A typical low-magnification, scanning transmission electron microscopy (STEM, details in Methods) image of the cross-section of a 14×14 superlattice, taken along the

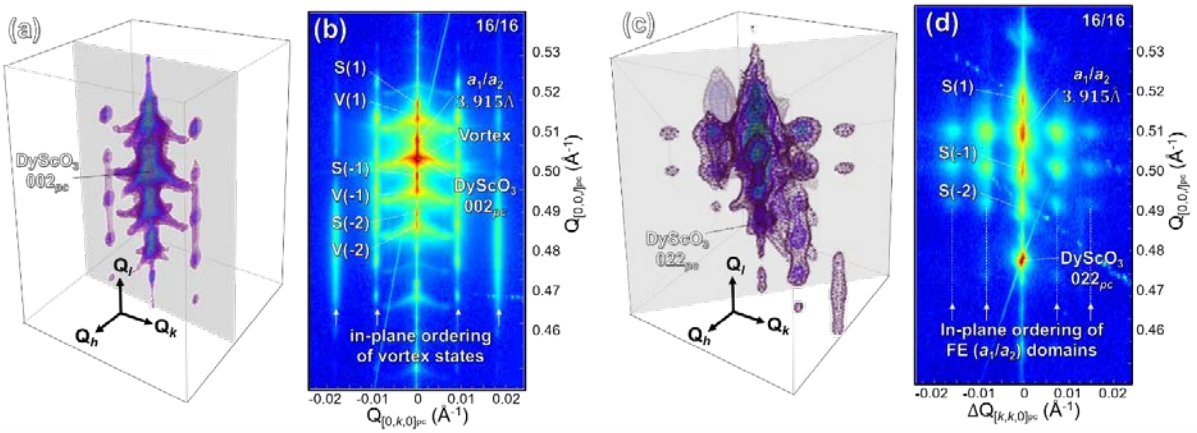

Supplementary Fig. 3. Synchrotron-based 3D-RSMs for a n =16 superlattice about the **a,** 002_{pc}-diffraction condition of the $DyScO_3$ substrate, and **b,** a planar section of this 3D-RSM containing the in-plane $[010]_{pc}$ and out-of-plane $[001]_{pc}$ showing an extra alloy peak, superlattice peaks, and characteristic in-plane satellites (periodicity ~11 nm) corresponding to the vortex phase. **c,** 3D-RSM about the off-axis 022_{pc}-diffraction condition of the $DyScO_3$ substrate, and **d,** a planar section of this 3D-RSM containing the in-plane $[110]_{pc}$ and out-of-plane $[001]_{pc}$ confirming the simultaneous presence of a_1/a_2 phase with an in-plane periodicity of ~13 nm.

$[010]_{pc}$ zone axis, reveals the layer uniformity (Supplementary Fig. 4a), and atomic-scale high-resolution STEM (HR-STEM) confirms sharp and coherent interfaces (Supplementary Fig. 4b). Mapping of the atomic polar displacement was performed to determine the polarization distribution within the superlattices. A displacement vector-mapping algorithm (details in Methods) was implemented on the cross-sectional HR-STEM images to measure local non-centrosymmetry of the lattice. A vector map of these polar displacements within a n = 14 superlattice heterostructure (Supplementary Fig. 4b) shows the formation of ordered arrays of vortex structures with alternating rotation directions, and is also illustrated in maps of the curl of the displacement vector field (Supplementary Fig. 4c). The lateral periodicity is approximately the same as the superlattice period (~11 nm).

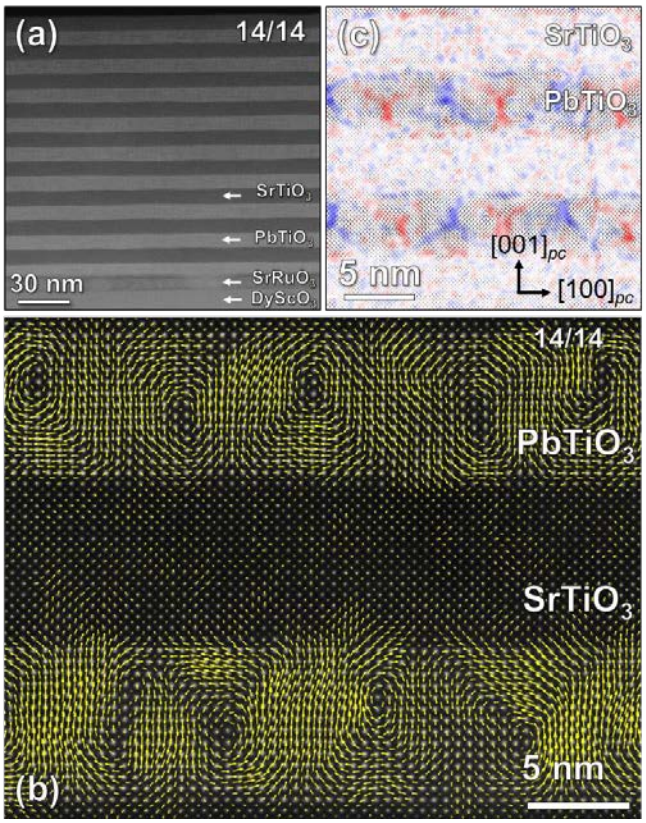

Supplementary Fig. 4. a, Typical low-magnification STEM image of the cross-section of a n = 14 superlattice taken along the $[010]_{pc}$ zone axis revealing layer uniformity. **b,** Atomic-scale, HR-STEM image showing sharp and coherent interfaces along with the overlaid vector map of polar displacements obtained from measurements of local non-centrosymmetry at the unit-cell level. **c,** Curl of the displacement vector field highlighting the formation of ordered arrays of vortex structures with alternating rotation directions.

3. Temperature-dependent synchrotron X-ray diffraction studies

Intermediate period superlattices possess a mixed-phase structure comprised of a_1/a_2 and vortex phases, which can be easily identified in X-ray diffraction studies (refer main text, Fig. 1a). To understand the nature of phase competition between the two phases, we conducted temperature-

dependent synchrotron X-ray diffraction θ-2θ line scans around the 002_{pc}-diffraction condition for both cooling and heating cycles (representative scans for heating cycle, Supplementary Fig. 5). The data is summarized in the form of intensity color maps (main text, Fig. 1e) and reveals a systematic conversion from vortex to a_1/a_2 phase upon heating along with the first-order nature of phase transition at ~250°C. Upon further heating, a subsequent phase transition from the a_1/a_2 phase to the paraelectric phase occurs at a higher temperature of ~327°C and is readily observed by tracking the dissappearance of satellite peaks corresponding to in-plane periodicity from the a_1/a_2 domains in the 3D-RSMs (planar section of the 3D-RSM around the off-axis 022_{pc}-diffraction condition containing the in-plane $[110]_{pc}$ and out-of-plane $[001]_{pc}$, Supplementary Fig. 6).

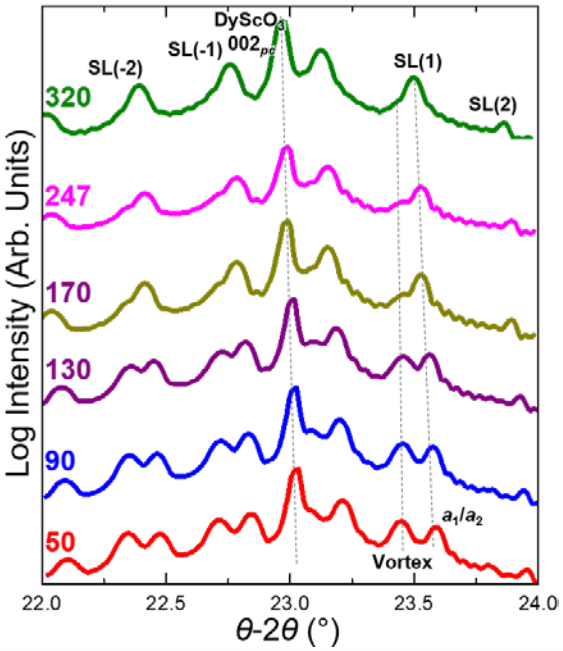

Supplementary Fig. 5. Temperature-dependent synchrotron X-ray θ-2θ line scan for an n = 16 superlattice about the 002_{pc}-diffraction condition of the $DyScO_3$ substrate revealing a systematic reduction (increase) in intensity of peaks corresponding to the vortex phase (a_1/a_2 phase) upon heating.

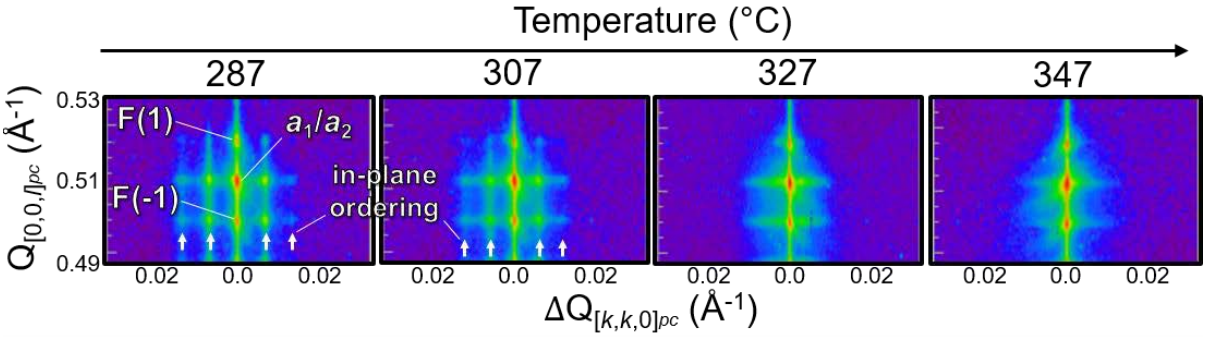

Supplementary Fig. 6. A planar section of the 3D-RSM about the off-axis 022_{pc}-diffraction condition revealing diminishing intensity of satellites from the a_1/a_2 domains upon heating, with an eventual transition to the paraelectric phase at ~327°C

4. Vectorial PFM studies

Synchrotron X-ray diffraction studies for the $n = 16$ superlattice reveal an ultrafine in-plane periodicity of ~13 nm for the a_1/a_2 phase. Since, the individual a domains are only 6-7 nm wide and are smaller than typical scanning-probe tips, PFM studies are unable to resolve them. Nevertheless, vectorial PFM studies can still be used to map the net equivalent polarization which is expected to be along the <110> for the a_1/a_2 superdomains, and thus can be used to identify the a_1/a_2 regions. In turn we obtained lateral PFM images with the scanning-probe cantilever along the $[110]_{pc}$ (Supplementary Fig. 7a) and $[010]_{pc}$ (Supplementary Fig. 7b). For scans with cantilever along the $[110]_{pc}$, the vortex regions and those a_1/a_2 superdomains that posses net polarization along the cantilever direction reveal near zero piezoresponse (brown regions), while those with orthogonal polarization exhibit high piezoresponse (black and white regions corresponding to left and right pointing polarization relative to the cantilever respectively, Supplementary Fig. 7a). For scans with cantilever along the $[010]_{pc}$, the net polarization of all a_1/a_2 superdomains are at 45° to the cantiliever and are epected to give a uniformly high contrast. In turn, they reveal a stripe-like order in which alternating stripes exhibit high (checkered black and white regions with left and right pointing polarization, respectively, relative to the cantilever) and low (brown) piezoresponse

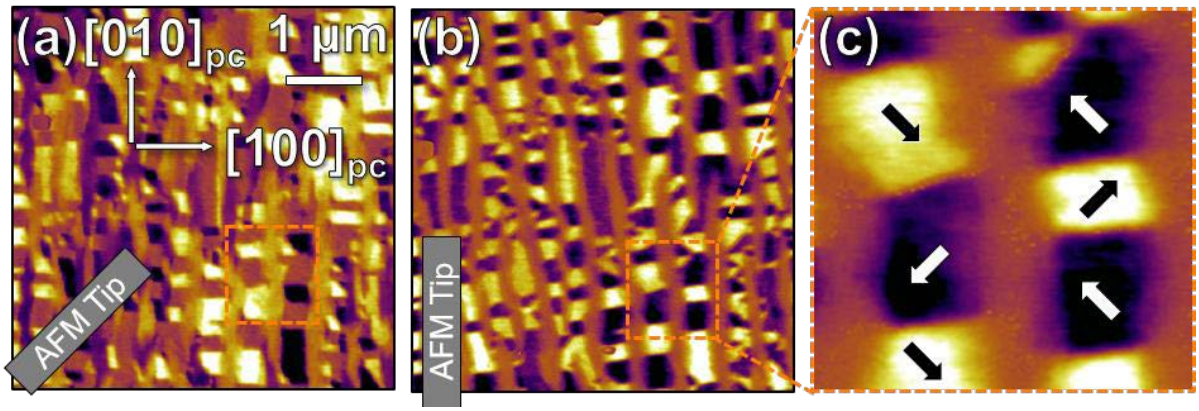

Supplementary Fig. 7. Lateral PFM images taken with the scanning-probe cantilever along the in-plane **a,** $[110]_{pc}$ and **b,** $[010]_{pc}$. **c,** Zoom-in of region within orange box and marked with arrows showing net in-plane polarization of a_1/a_2 superdomains (obtained by a vectorial combination of lateral PFM responses).

with a periodicity of ~300 nm along the $[010]_{pc}$ (Supplementary Fig. 7a). Each stripe exhibiting an overall low piezoresponse, in both lateral PFM images (Supplementary Fig. 7a and b), corresponsds to the vortex phase. The other stripes, possesing high piezoresponse, correspond to the a_1/a_2 regions, and their net polarization can be mapped by a vectorial combination (Supplementary Fig. 7c) of the lateral PFM images obtained.

5. Second-principles simulations

Second-principles simulations were completed for an n = 14 superlattice (see Methods for details) and confirm the formation of vortex arrays as the ground-state structure [Supplementary Fig. 8; wherein green (black) arrows represent a projection of the local dipoles normal to $[100]_{pc}$ (the vortex axis) that is computed on the elemental perovskite unit cells centered on Pb (Ti)]. The color map reveals an axial component of the polarization along the $[100]_{pc}$ (vortex axis), and reveals the formation of oppositely pointing blue and red domains. The existence of such an axial component is robust, and it appears naturally during the thermal Monte Carlo simulations even when absent in the initial configuration. At the same time, there are a large number of local minima that are essentially degenerate in energy, and it is found that the axial component of polarization in adjacent vortices can point in the same or opposite directions. Under such a scenario, one can expect the direction of the axial component of polarization in the vortex

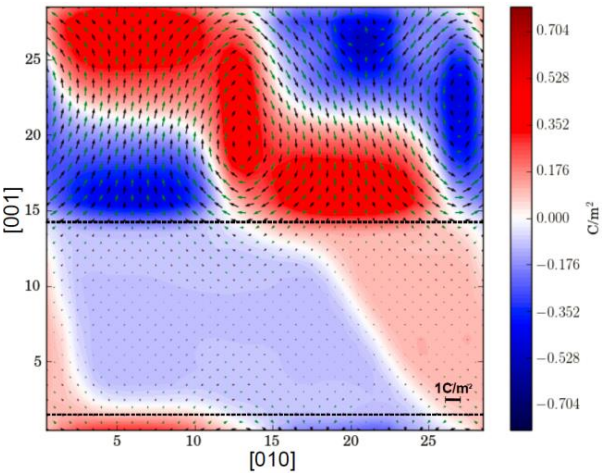

Supplementary Fig. 8. Second-principles simulation showing vortex arrays in an n=14 superlattice. Green (black) arrows represent, the projection of the local dipoles normal to the $[100]_{pc}$ (vortex axis) that is computed on the elemental perovskite unit cells centered on Pb (Ti). The color map corresponds to the polarization component along $[100]_{pc}$ (vortex axis).

phase to be set by the adjacent ferroelectric domains, as observed from phase-field and piezoresponse studies (main text Fig. 3).

6. Electric-field control for ferroelectric and toroidal phases

PFM-based switching studies were completed to demonstrate electric-field control of the ferroelectric and vortex phases. Just as the application of a positive 15 V bias (via a scanning probe tip within the orange box, main text Fig. 5a) resulted in the mixed-phase structure being converted to one with a uniformly low piezoresponse corresponding to the vortex state (main text Fig. 5b), an equivalent conversion can also be obtained upon application of a negative electrical bias. Akin to what is reported in the main text, starting from a mixed-phase structure (Supplementary Fig. 9a), application of a negative bias using a PFM tip converts the region in the orange box to a pure vortex phase with uniformly low piezoresponse (Supplementary Fig. 9b). Furthermore, phase-field based application of a negative bias to the mixed-phase structures (the same as main text Fig. 4b) and subsequent relaxation, also demonstrates such conversion to a pure vortex phase (Supplementary Fig. 9c).

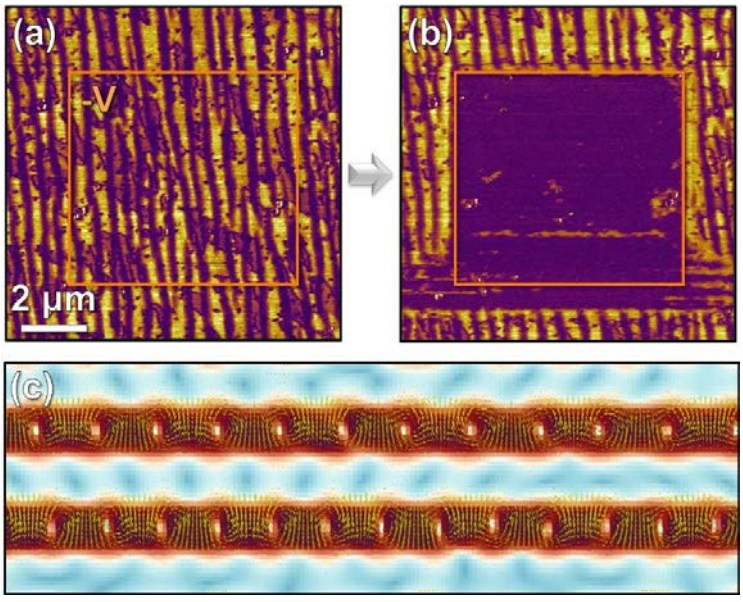

Supplementary Fig. 9. Piezoresponse force microscopy (lateral amplitude) images for the (a) as-grown, mixed-phase structures with an orange box outlining the area to be poled with a -18 V bias and (b) the resulting conversion of the material to a pure vortex structure in this poled region. (c) Final equilibrium vortex structure predicted by phase-field simulations after applying a negative bias and allowing the sample to relaxation in exactly the same fashion as the data in Figure 4 of the main text.

The back conversion from the pure vortex phase to the mixed-phase structures is possible by

exploiting the in-plane component of the electric field from the PFM tip. This capability (*i.e.*, the regeneration of stripes of a_1/a_2 within the pure vortex region, main text Fig. 5c) has been demonstrated in the main text, but needs further elaboration. Again, starting from a region which has been poled to be purely vortex in nature (main text Fig. 5b, and reproduced here as Supplementary Fig. 10a), we can apply negative bias in a line pattern. Upon applying a negative bias to the tip results in regions directly under the tip that have contrast consistent with the low piezoelectric response of the vortex phase (highlighted with arrows, Supplementary Fig. 10b). Adjacent to these written lines, one can observe high response consistent with the a_1/a_2 phase where the in-plane fields from the tip are the strongest.

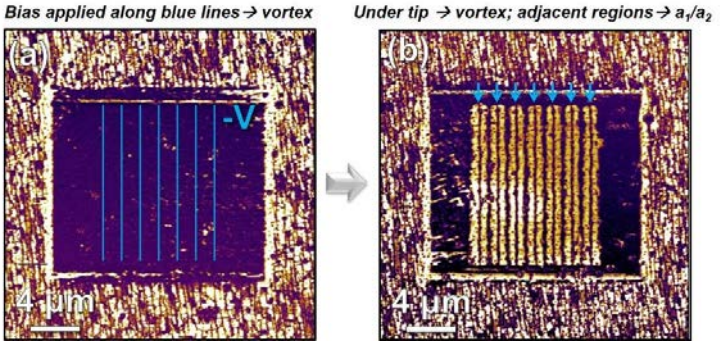

Supplementary Fig. 10. Piezoresponse force microscopy (lateral amplitude) images for the (a) positive voltage poled, pure vortex region of the sample and (b) the resulting conversion of the material back to a mixed-phase structure with in-plane polarized a_1/a_2 structures upon application of -15 V bias. Note that directly under tip where the bias was applied the sample remains vortex in nature, but in adjacent regions where there is significant in-plane field component the a_1/a_2 structures are produced.

7. Synchrotron X-ray nanodiffraction studies

X-ray diffraction microscopy was performed to probe electric-field driven reversible switching between the ferroelectric a_1/a_2 phase and the vortex phase for an n =16 superlattice. These two coexisting phases possess a distinct set of alloy, superlattice, and satellite peaks, and are easily differentiated in X-ray RSMs (main text Fig. 1c). For the nanodiffraction studies, we focus on diffraction intensities at two regions of interest (ROI) in the reciprocal space: one at the 002_{pc}-diffraction peak for the a_1/a_2 phase, and the other at the satellite peak position of the vortex

phase (black boxes labeled I(a_1/a_2) and I(V), respectively, Supplementary Fig. 11a) to provide a structural map of the same location as those explored in PFM studies (main text Figs. 5b,c). In the low piezoresponse region obtained by applying positive 15 V (main text, Fig. 5b), the nanodiffraction intensity from the a_1/a_2 phase (inset, main text Fig. 5b) is found to decrease along with a simultaneous increase in the intensity of the vortex satellite peak (Supplementary Fig. 11b). Again, upon poling back to the mixed-phase structure (main text Fig. 5c), features corresponding to alternating a_1/a_2 and vortex phases appear in the nanodiffraction images (inset of main text Fig. 5c and Supplementary Fig. 11c). A wide range θ-2θ scan (Supplementary Fig. 11d) at the pure vortex region (spot 1, Supplementary Fig. 11b), we observe a single set of alloy and superlattice diffraction peaks (red data, Supplementary Fig. 11d) along with emergence of the characteristic

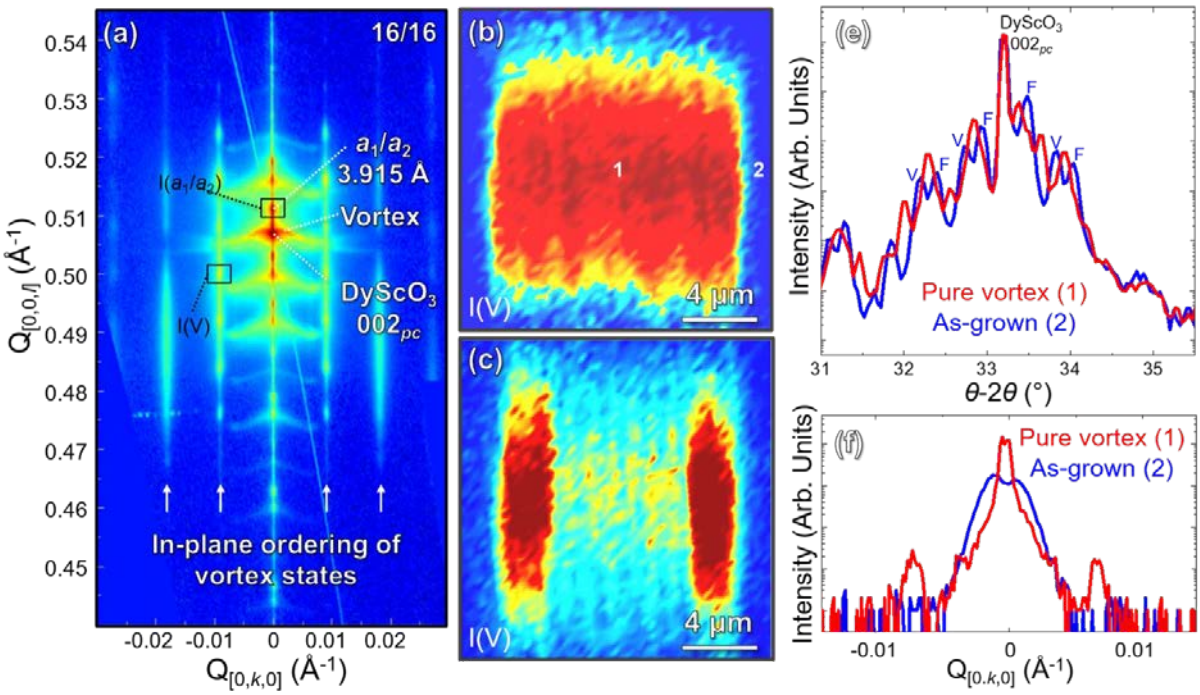

Supplementary Fig. 11. a, A section of 3D-RSM around 002_{pc} peak of the $DyScO_3$ substrate for an n = 16 superlattice heterostructure. The box labeled I(a_1/a_2) is used to integrate signal for probing the ferroelectric a_1/a_2-phase fraction and yields nanodiffraction images shown in the main text (inset, Figs. 5e,f). Corresponding nanodiffraction images obtained by integrating the signal from the box labeled I(V) instead, results in **b**, and **c,** which represent a measure of the vortex phase fraction at these respective locations. **d**, Wide range θ-2θ line scans at locations 1 (red data) and 2 (blue data) reveal the electric-field-driven transformation from a mixed-phase structure to pure vortex phase. **e,** Q-scans along the $[010]_{pc}$ at the same two locations confirming the presence of satellites characteristic of the vortex phase at location 1 (red data).

in-plane satellite peaks of the vortex phase (red data, Supplementary Fig. 11e). This is in contrast to the split peaks from the coexistence of vortex and a_1/a_2 phases (blue data, Supplementary Fig. 11d) observed in the as-grown region (spot 2, Supplementary Fig. 11b). In turn, these studies confirm the electric-field-driven conversion from mixed-phase structure into the vortex phase, and back to the mixed-phase configuration as observed in the piezoresponse studies (main text Fig. 5).

8. Synchrotron photoemission electron microscopy (PEEM)

PEEM XLD contrast images (spatial resolution of 30 nm, Supplementary Fig. 12a) for an n =16 superlattice reveal spectroscopic signatures of the mixed-phase structures. Here, we focus on poled areas (obtained following procedures as per main text Fig. 5c) that simultaneously possess regions showing the as-grown mixed-phase structure (blue box, Supplementary Fig. 12a and Supplementary. Fig. 12b), regions poled to the pure vortex phase (areas with uniformly bright contrast, Supplementary Fig. 12a), and a region that was poled back to the mixed-phase structure (red box, Supplementary Fig. 12a and Supplementary. Fig. 12b). Thresholded images (Supplementary Fig. 12d and e) corresponding to the PEEM contrast for the as-grown and poled mixed-phase regions (Supplementary Fig. 12d and e, respectively), were used to compute the XLD difference spectra of the as-grown and poled mixed-phase regions (Supplementary Fig. 12f and g, respectively). The linear dichroism of the Ti L_3 t_{2g} orbitals at 458 eV is the result of the different [100] ferroelectric polarization component of the two phases; the e_g dichroism at 460 eV is comparatively weak. The similarity in the dichroism spectra and the similar level of contrast in the images indicate a similar polarization structure of the as-grown and poled mixed-phase regions, implying that the vortex phase created by poling is identical to the initial as-grown vortex phase. The XLD images also show that the positive-bias-poled region was uniformly transformed into

the vortex state except for small defects since it shows the same bright contrast as the lighter stripe-like features in both mixed phase areas.

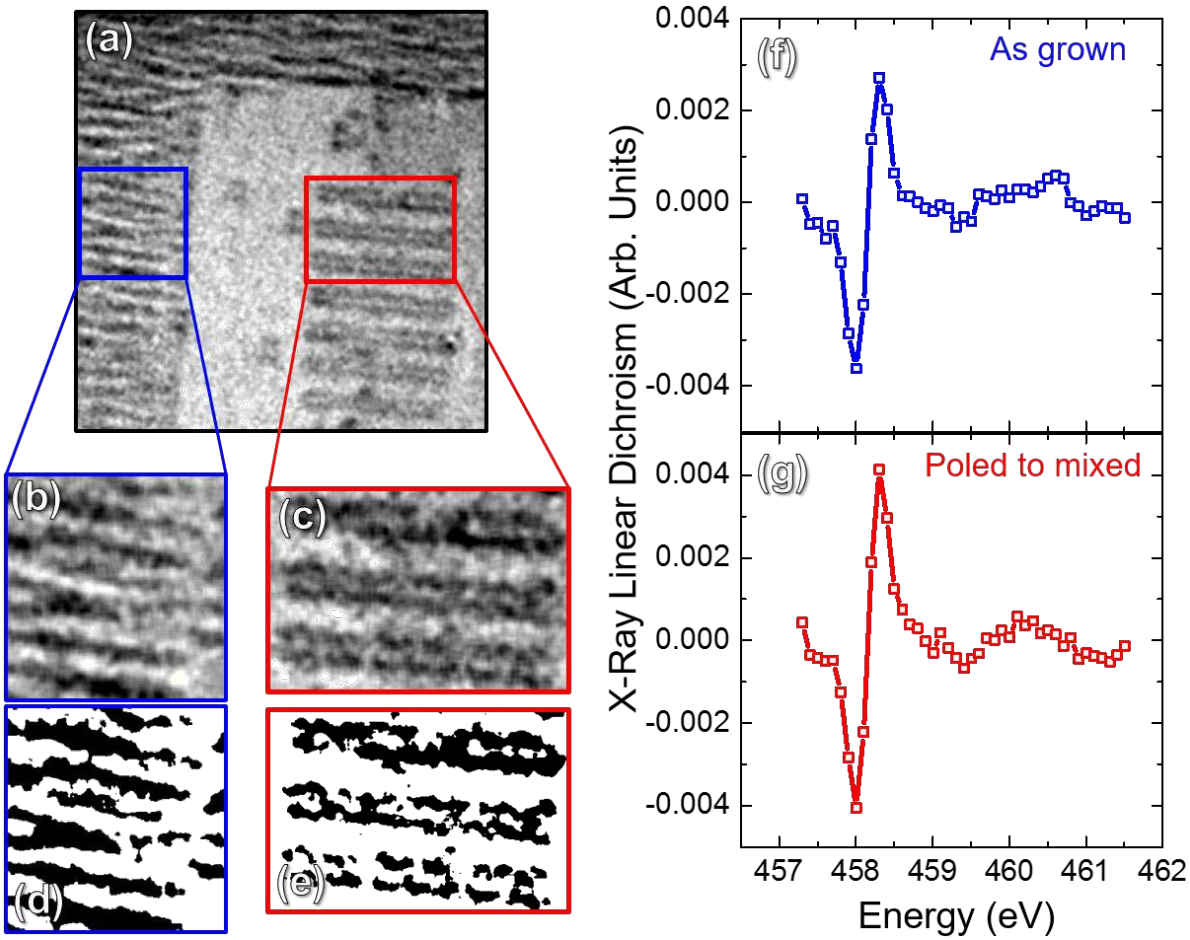

Supplementary Fig. 12. a, PEEM XLD contrast image of a poled area on an n =16 superlattice. We focus on regions highlighted in the blue and red box in this figure corresponding to regions with **b,** the as-grown, mixed-phase structure, and **c,** a region that was poled back to the mixed-phase state, respectively. PEEM contrast-based thresholded images for **d,** the as-grown and **e,** the poled mixed-phase regions were used to compute the XLD difference spectra of **f,** the as-grown and **g,** the poled mixed-phase regions.

9. Second harmonic generation (SHG) studies

The non-linear optical responses of the ferroelectric a_1/a_2 and the vortex phases were studied using far-field SHG measurements in reflection mode geometry (Methods) with polar plots for S_{in}/S_{out} and S_{in}/P_{out} configurations (Supplementary Fig. 13, orange and green data, respectively). The studies were completed for as-grown regions and regions that were poled to the pure vortex

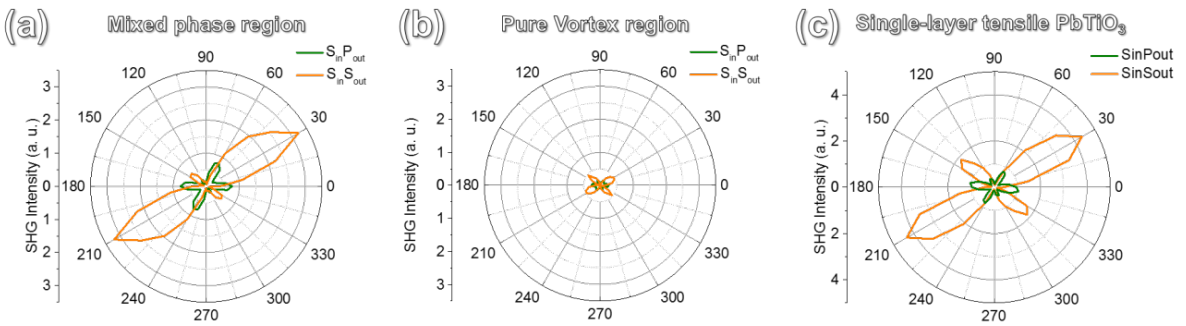

Supplementary Fig. 13. SHG polar plots obtained from regions with the **a,** as-grown mixed-phase structure, **b,** the electrically-poled pure vortex structure, and **c,** a tensile-strained $PbTiO_3/SmScO_3$ (110) thin film possessing in-plane polarized a_1/a_2 ferroelectric domain structure.

phase on a representative n =16 superlattice (Supplementary Figs. 13a and b, respectively), as well as a single-layer $PbTiO_3$ film grown on a $SmScO_3$ (110)$_O$ substrate possessing an a_1/a_2 domain structure (Supplementary Fig. 13c). The symmetries of the polar plots obtained from the as-grown regions match well with those from the single-layer $PbTiO_3$ films indicating predominant contributions from the ferroelectric a_1/a_2 phase. A highly diminished response is observed from the vortex regions as is indicative of the reduced anisotropy in the vortex-phase as compared to the ferroelectric phase.

References

1 Pertsev, N. A. & Zembilgotov, A. G. Energetics and geometry of 90° domain structures in epitaxial ferroelectric and ferroelastic films. *Journal of Applied Physics* **78**, 6170-6180 (1995).